Received: 20 January 2019 | Accepted: 22 January 2019

DOI: 10.1002/asna.201913604

ORIGINAL ARTICLE

Astronomische Nachrichten

Magnetic helicity and fluxes in an inhomogeneous α^2 dynamo

A. Brandenburg[1,2,3,4,*]

[1]Nordita, KTH Royal Institute of Technology, Stockholm University, Stockholm, Sweden
[2]Department of Astronomy, Stockholm University, Stockholm, Sweden
[3]JILA, Laboratory for Atmospheric and Space Physics, University of Colorado, Boulder, Colorado
[4]Department of Physics, McWilliams Center for Cosmology, Carnegie Mellon University, Pittsburgh, Pennsylvania

***Correspondence**
A. Brandenburg, Nordita, KTH Royal Institute of Technology and Stockholm University, Stockholm 10691, Sweden.
Email: brandenb@nordita.org

Funding Information
University of Colorado. NSF Astronomy a Astrophysics Grants Program, 1615100.

Much work on turbulent three-dimensional dynamos has been done using triply periodic domains, in which there are no magnetic helicity fluxes. Here, we present simulations where the turbulent intensity is still nearly homogeneous, but now there is a perfect conductor boundary condition on one end and a vertical field or pseudovacuum conditions on the other. This leads to migratory dynamo waves. Good agreement with a corresponding analytically solvable α^2 dynamo is found. Magnetic helicity fluxes are studied in both types of models. It is found that at moderate magnetic Reynolds numbers, most of the magnetic helicity losses occur on large scales. Whether this changes at even larger magnetic Reynolds numbers, as required for alleviating the catastrophic dynamo quenching problem, remains still unclear.

KEYWORD
magnetic fields – magnetohydrodynamics – turbulence

1 | INTRODUCTION

Stars like the Sun possess large-scale magnetic fields that are believed to be generated by an α effect, which amplifies the magnetic field and sustains it against turbulent diffusive decay (Rüdiger & Hollerbach 2004). Together with differential rotation, it can lead to cyclic magnetic fields and equatorward migration (Parker 1955). The theoretical "butterfly" diagram of the mean toroidal magnetic field versus time and latitude is similar to that observed (Steenbeck & Krause 1969).

The theory of the α effect of Steenbeck et al. (1966) is based on a kinematic treatment, so the velocity field is assumed given. Not only are the velocity fluctuations given, but one also assumes that the magnetic fluctuations are entirely the result of tangling of the large-scale magnetic field. This is justified at small magnetic Reynolds numbers ($\mathrm{Re_M} \ll 1$, corresponding to low electrical conductivity) or in cases when the turbulence has a short correlation time. The latter is an artificial construct, because real turbulence always has a finite correlation time. Therefore, the theory was always known to be problematic under astrophysically relevant conditions when $\mathrm{Re_M} \gg 1$ and the correlation time finite.

Significant progress was made by Pouquet et al. (1976), who extended the theory of the α effect to a fully dynamical one, where α attains a magnetic contribution corresponding to the swirl of the magnetic field or, more precisely, the current helicity of the small-scale magnetic field. Their work also emphasized the importance of magnetic helicity conservation, leading to an inverse cascade of magnetic helicity toward large scales, but no explicit connection was drawn between the current helicity of the small-scale field contributing to the α effect and the large-scale magnetic field, as it builds up at the same time.

In an important article reported by Kleeorin & Ruzmaikin (1982), the gap between the current helicity contribution to the α effect and the actual large-scale magnetic field was closed. At that time, however, the focus was on the possibility of chaos resulting from such a feedback (Ruzmaikin 1981), a topic that was just introduced into solar physics by Tavakol (1978).

Then, in the early 1990s, dynamo theory experienced a crisis with the work of Cattaneo & Vainshtein (1991) and Vainshtein & Cattaneo (1992), who found that turbulent diffusion and α effect are "catastrophically" quenched, that is, they are quenched in an $\mathrm{Re_M}$-dependent fashion. In a series of articles, Gruzinov & Diamond (1994, 1995, 1996) developed an explanation in terms of magnetic helicity conservation. Using turbulent dynamo simulations in periodic domains, Brandenburg (2001) found large-scale magnetic fields in excess of the equipartition value, but the ultimate nonlinear saturation

phase lasted a microphysical diffusion time, which would be very long in astrophysical applications. It was only with the works of Field & Blackman (2002), Blackman & Brandenburg (2002), and Subramanian (2002) that it became clear that the relevant theory describing such a quenching is that of Kleeorin & Ruzmaikin (1982).

Unfortunately, the authors of this early work did not consider the somewhat academic case of a homogeneous system, which was what Cattaneo & Hughes (1996) simulated. They found a suppression of α proportional to $1/(1+Re_{\rm M}\overline{\boldsymbol{B}}^2/B_{\rm eq}^2)$, suggesting that, in a saturated state, $|\overline{\boldsymbol{B}}|$ would only be a fraction ${\rm Re_M}^{-1/2}$ of the equipartition field strength $B_{\rm eq}$. In an inhomogenous system, magnetic helicity fluxes are possible, and those were already included in the theory of Kleeorin & Ruzmaikin (1982), but whether this really alleviates the catastrophic quenching problem remains unclear even today. It is a hard problem, because even at magnetic Reynolds numbers of 1000, resistive contributions are still comparable to those of the magnetic helicity flux (Del Sordo et al. 2013; Hubbard & Brandenburg 2010; Mitra et al. 2010).

The basic idea of invoking magnetic helicity fluxes is the following. As the α effect builds up a large-scale magnetic field, it also builds up magnetic helicity associated with this large-scale field. In the absence of magnetic helicity fluxes, small-scale magnetic helicity of a sign opposite to that of the large-scale field must be produced to obey total magnetic helicity conservation. This is indeed what Seehafer (1996) and Ji (1999) found using independent approaches. The current helicity associated with small-scale magnetic helicity quenches the dynamo prematurely. Thus, to alleviate this quenching, small-scale magnetic helicity must be removed preferentially. This was demonstrated by Brandenburg et al. (2002) in what they called a "vacuum cleaner" experiment, in which they removed all the small-scale magnetic field from a simulated dynamo in regular intervals. They found that this allows the field to saturate at a new level with a stronger magnetic field.

The purpose of the present article is to give an update on this situation and to present new results of a model of an inhomogeneous dynamo that may be suitable for addressing the problem of catastrophic quenching. In particular, we will use an α^2 dynamo that is made inhomogeneous through the introduction of different boundary conditions on opposite ends of the domain: a perfect connector (PC) boundary condition on the lower end and a quasi-vacuum or vertical field (VF) condition on the upper. This leads to an oscillatory α^2 dynamo with dynamo waves migrating away from the PC boundary to the VF boundary. This is a system for which an analytic solution exists (Brandenburg 2017). Helicity fluxes of such a model were first studied using a mean field model that incorporates magnetic helicity conservation (Brandenburg et al. 2009, hereafter BCC).

The results of BCC remained puzzling in view of our understanding so far, because they found that the flux of magnetic helicity on large and small length scales was equally strong and of opposite sign. This did not fit the expectation that there should be a preferential loss of small-scale magnetic helicity. Things became even more confusing when they found that the magnetic helicity ejected into the halo outside the dynamo region has the wrong sign; see the last panel of Figure 7 of BCC. Two years later, it was found that the magnetic helicity in the solar wind at a distance of 1–5 AU from the Sun also has the wrong sign (Brandenburg et al. 2011). Even today, there is no clear understanding of what this means in view of the idea of alleviating catastrophic quenching by preferential small-scale magnetic helicity losses.

The model of BCC has never been tested in a direct numerical simulation (DNS). This will be done in the present article. We begin by presenting the model and then report results from the magnetic helicity fluxes in the resistive Weyl gauge (Candelaresi et al. 2011), which is convenient for numerical purposes, although the results may a priori be gauge-dependent.

2 | THE MODEL

We use DNS similar to the homogeneous models of Brandenburg (2001) and the inhomogeneous ones of Brandenburg & Dobler (2001), except that here we have a PC boundary condition at $z=0$ and a VF condition at $z=\pi/2$. Such a choice was already adopted by BCC, and this size of the domain was chosen because the eigenfunctions of the free decay problem are quarter sine wave with wavenumber $k_1=1$. In other words, the decay rate, $\eta_{\rm t}k_1^2$, with a turbulent diffusivity $\eta_{\rm t}=1$ is then also unity. We choose here a cubic domain, so its size is $(\pi/2)^3$.

We adopt an isothermal equation of state, so the pressure p is proportional to the density ρ with $p=\rho {c_{\rm s}}^2$, where $c_{\rm s}$ is the isothermal sound speed. We advance the magnetic vector potential $\boldsymbol{A}$ for the magnetic field $\boldsymbol{B}=\boldsymbol{\nabla}\times\boldsymbol{A}$, and solve the uncurled induction equation, the momentum equation for the velocity $\boldsymbol{U}$, and the continuity equation for $\ln\rho$, so we have the following system of equations:

$$\frac{\partial \boldsymbol{A}}{\partial t}=\boldsymbol{U}\times\boldsymbol{B}+\eta\nabla^2\boldsymbol{A}, \tag{1}$$

$$\rho\frac{{\rm D}\boldsymbol{U}}{{\rm D}t}=\boldsymbol{J}\times\boldsymbol{B}+\nabla\cdot(2\nu\rho\boldsymbol{\mathsf{S}})-c_{\rm s}^2\nabla\rho+\rho\boldsymbol{f}, \tag{2}$$

$$\frac{{\rm D}\ln\rho}{{\rm D}t}=-\nabla\cdot\boldsymbol{U}, \tag{3}$$

where $\boldsymbol{J}=\boldsymbol{\nabla}\times\boldsymbol{B}$ is the current density in units where the vacuum permeability is unity, $\mathsf{S}_{ij}=\frac{1}{2}(\partial_i u_j+\partial_j u_i)-\frac{1}{3}\delta_{ij}\nabla\cdot\boldsymbol{u}$ are the components of the traceless rate-of-strain tensor, ν and η are the kinematic viscosity and magnetic diffusivity, respectively, and $\boldsymbol{f}$ is a monochromatic forcing function that is δ-correlated in time and fully helical so that $\boldsymbol{\nabla}\times\boldsymbol{f}\approx-k_{\rm f}\boldsymbol{f}$, that is, the helicity is negative and $k_{\rm f}$ is the average forcing wavenumber. We choose $k_{\rm f}=16\,k_1$, which corresponds to 4 full wavelengths across the $\pi/2$ domain.

In most of our simulations, the helicity of the forcing is uniform, but in one case we adopt a modulation of the helicity

TABLE 1 Parameters of the runs, their end times t_e, and the number of time steps n_t in millions (M) and the number of mesh points

Run	$\mathrm{Re_M}$	$u_{\rm rms}k_{\rm f}t_{\rm e}$	$\eta_{\rm t0}k_1^2t_{\rm e}$	$\eta k_1^2t_{\rm e}$	n_t (M)	Mesh
G	170	7000	9.1	0.16	3	288^3
A	180	14,000	18.2	0.30	6	288^3
B	370	2700	3.5	0.028	2.3	576^3
C	750	300	0.4	0.0016	0.5	1152^3

proportional to $\cos k_1 z$. Thus, the helicity is then maximum at $z=0$, and goes to zero at the boundary at $k_1 z=\pi/2$.

Our simulations are characterized by the magnetic Reynolds and magnetic Prandtl numbers,

$$Re_{\rm M}=u_{\rm rms}/\eta k_{\rm f},\quad \mathrm{Pr_M}=\nu/\eta, \tag{4}$$

respectively, where $u_{\rm rms}=\langle \boldsymbol{u}^2\rangle^{1/2}$ is the root-mean squared (rms) velocity and angle brackets denote volume averages. By contrast, horizontal or xy averages will be denoted by overbars. In this work we always take $\mathrm{Pr_M}=1$.

The magnetic field is often expressed in terms of the equipartition field strength, $B_{\rm eq}=\sqrt{\rho}u_{\rm rms}$. We usually express time in turbulent–diffusive times, $\tau_{\rm td}=(\eta_{\rm t0}k_1^2)^{-1}$, where $\eta_{\rm t0}=u_{\rm rms}/3k_{\rm f}$ is an approximation to the turbulent magnetic diffusivity (Sur et al. 2008). By comparison, the turnover time is $\tau_{\rm to}=(u_{\rm rms}k_{\rm f})^{-1}$, which is shorter by the square of the scale separation or, more precisely, $\tau_{\rm to}/\tau_{\rm td}=3(k_{\rm f}/k_1)^2=768$. Furthermore, the resistive time $\tau_\eta=(\eta k_1^2)^{-1}$ is longer than the turbulent–diffusive time by one third of the magnetic Reynolds number, that is, $\tau_\eta/\tau_{\rm td}=\mathrm{Re_M}/3$.

3 | RESULTS

We consider three different Reynolds numbers using three different resolutions. Our model A with $\mathrm{Re_M}=180$ and a resolution of 288^3 mesh points reaches full saturation and develops magnetic cycles with periods on the scale of the turbulent–diffusive time, while models B and C with higher $\mathrm{Re_M}$ and higher resolution have not fully saturated. In addition, we present a model with a gradient of the helicity and hence a gradient of the underlying α effect (model G), which has otherwise similar parameters as model A. In fact, Run G was the progenitor of Run A. All runs, along with their end time $t_{\rm e}$, expressed in different ways, and their resolution are listed in Table 1.

3.1 | Magnetic field growth and saturation

We usually start with a random magnetic field that is δ-correlated in space. This has the advantage that the dynamo quickly develops exponential growth after the first 100 turnover times, or the first 0.2 turbulent–diffusive times; see Figure 1. In the present runs, the exponential growth phase is not well developed because the initial field was already relatively strong. In fact, it is initially close to equipartition, but,

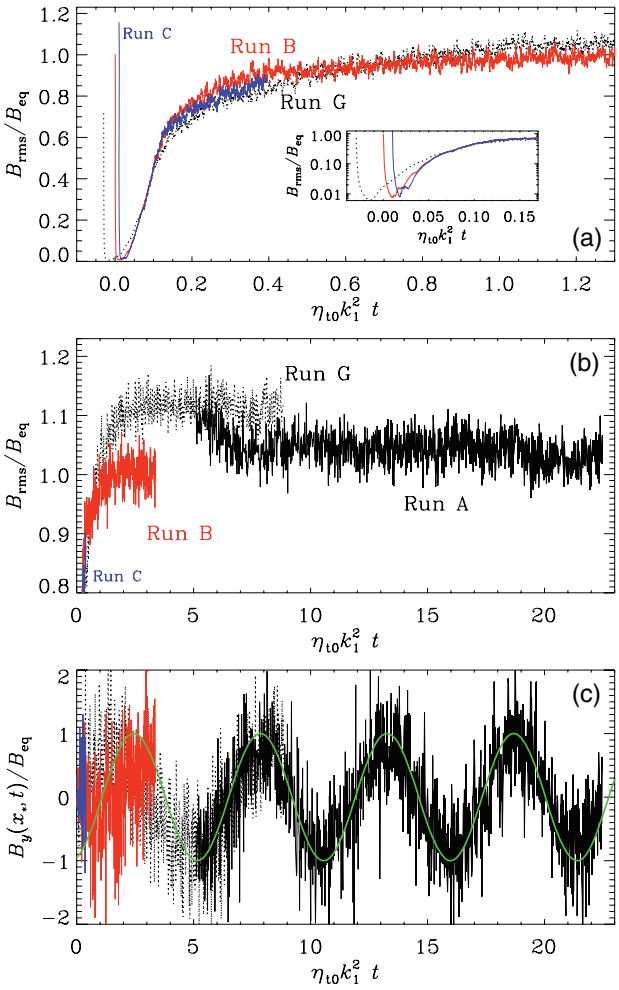

FIGURE 1 Comparison of $B_{\rm rms}/B_{\rm eq}$ during the early saturation phase for Runs G, B, and C (a), the later development and restarting of Run A from Run G at $\eta_{\rm t0}k_1^2t\approx5$, and comparison with Runs B and C (b), and the establishment of magnetic cycles seen in the magnetic field at one point $\boldsymbol{x}=\boldsymbol{x}_*$ in the lower part of the domain with frequency $\omega=1.16\eta_{\rm t0}k_1^2$ (c)

being δ-correlated in space, most of the field is in the diffusive subrange and so the rms field drops by a factor of a hundred before the dynamo sets in.

We can cautiously estimate the growth rate to be $\lambda\approx0.09u_{\rm rms}k_{\rm f}\approx70\eta_{\rm t0}k_1^2$. This is about three times faster than the typical growth rate of a mildly supercritical small-scale dynamo, suggesting that it is a hybrid between a small-scale and a large-scale dynamo. The growth rates of such hybrid dynamos unifying small-scale and large-scale dynamos were studied by Subramanian & Brandenburg (2014) and Bhat et al. (2016) for a range of different values of $\mathrm{Pr_M}$. They used, however, periodic boundary conditions, for which the time for establishing a large-scale field is the resistive time (Brandenburg 2001).

In addition to the total (small-scale plus large-scale) magnetic field reaching rapid saturation without a prolonged nonlinear saturation phase, as in Brandenburg (2001) and Candelaresi & Brandenburg (2013), also the space–time properties of the large-scale magnetic field are found to develop quickly. This is shown in Figure 2, where we compare

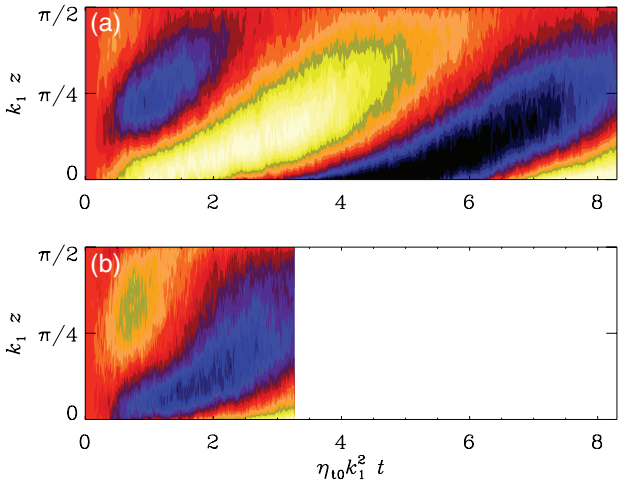

FIGURE 2 Butterfly diagrams of $\overline{B}_y(z,t)$ for Runs G (a) and B (b) during the first eight turbulent–diffusive times. Note that in both cases a large-scale field is clearly visible after a fraction of the turbulent–diffusive time

butterfly diagrams for Run G with $\mathrm{Re_M} = 170$ and Run B with $\mathrm{Re_M} = 370$. In both cases, the large-scale field is clearly visible even after just one turbulent–diffusive time, or even earlier. Nevertheless, the rms magnetic field is still growing, as can be seen from Figure 1. Unfortunately, such runs are getting computationally rather costly and even after 2.3 million time steps they have not run for long enough to see a well-developed cycle.

3.2 | Butterfly diagrams for other fields

In Figure 3, we present butterfly diagrams of $\overline{A}_x$, $\overline{A}_y$, $\overline{B}_x$, $\overline{B}_y$, $\overline{J}_x$, and $\overline{J}_y$. All panels show clear signs of the magnetic cycle. However, $\overline{J}_x$ and $\overline{J}_y$ are rather "noisy," which is connected with the fact that they are related to higher derivatives of $\boldsymbol{A}$ and $\boldsymbol{B}$.

Note that, because of $\nabla \cdot \overline{\boldsymbol{B}} = \nabla \cdot \overline{\boldsymbol{J}} = 0$, and because there is no mean flux, we have $\overline{B}_z = \overline{J}_z = 0$. In our case $\nabla \cdot \overline{\boldsymbol{A}}$ does not vanish, so $\overline{A}_z$ does not vanish either, it does not display any cyclic variations and is not of physical interest because it does not contribute to $\overline{\boldsymbol{B}}$. We return to the discussion of $\boldsymbol{\nabla \cdot A}$ in connection with magnetic helicity fluxes, but even then it will turn out to be unimportant.

The large-scale magnetic field varies in the z direction and is roughly described by what is expected based on the analytic mean-field theory. It is useful to express the mean magnetic

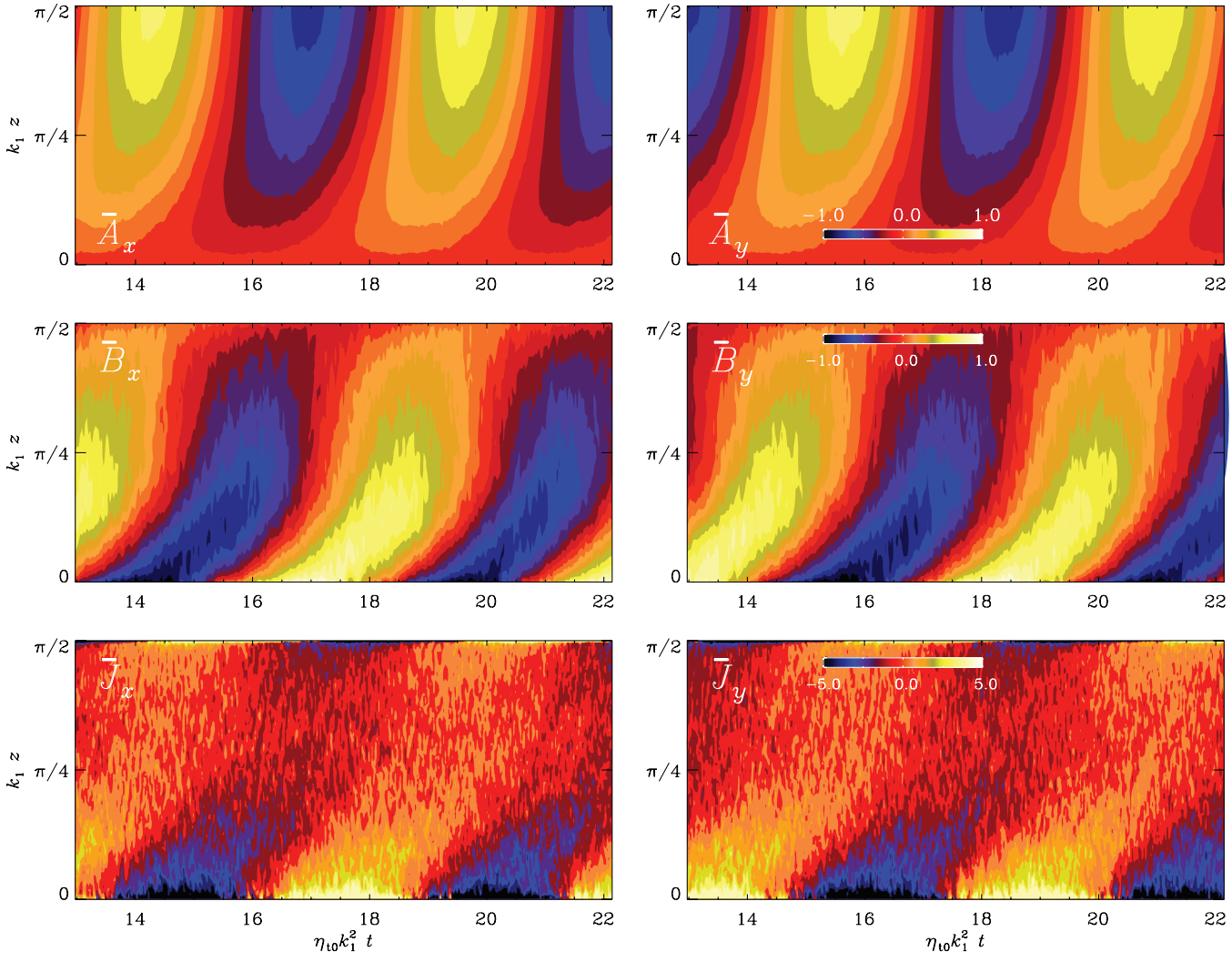

FIGURE 3 Butterfly diagrams of $\overline{A}_x$, $\overline{A}_y$, $\overline{B}_x$, $\overline{B}_y$, $\overline{J}_x$, and $\overline{J}_y$ for Run A, covering almost two cycles near the end of the run

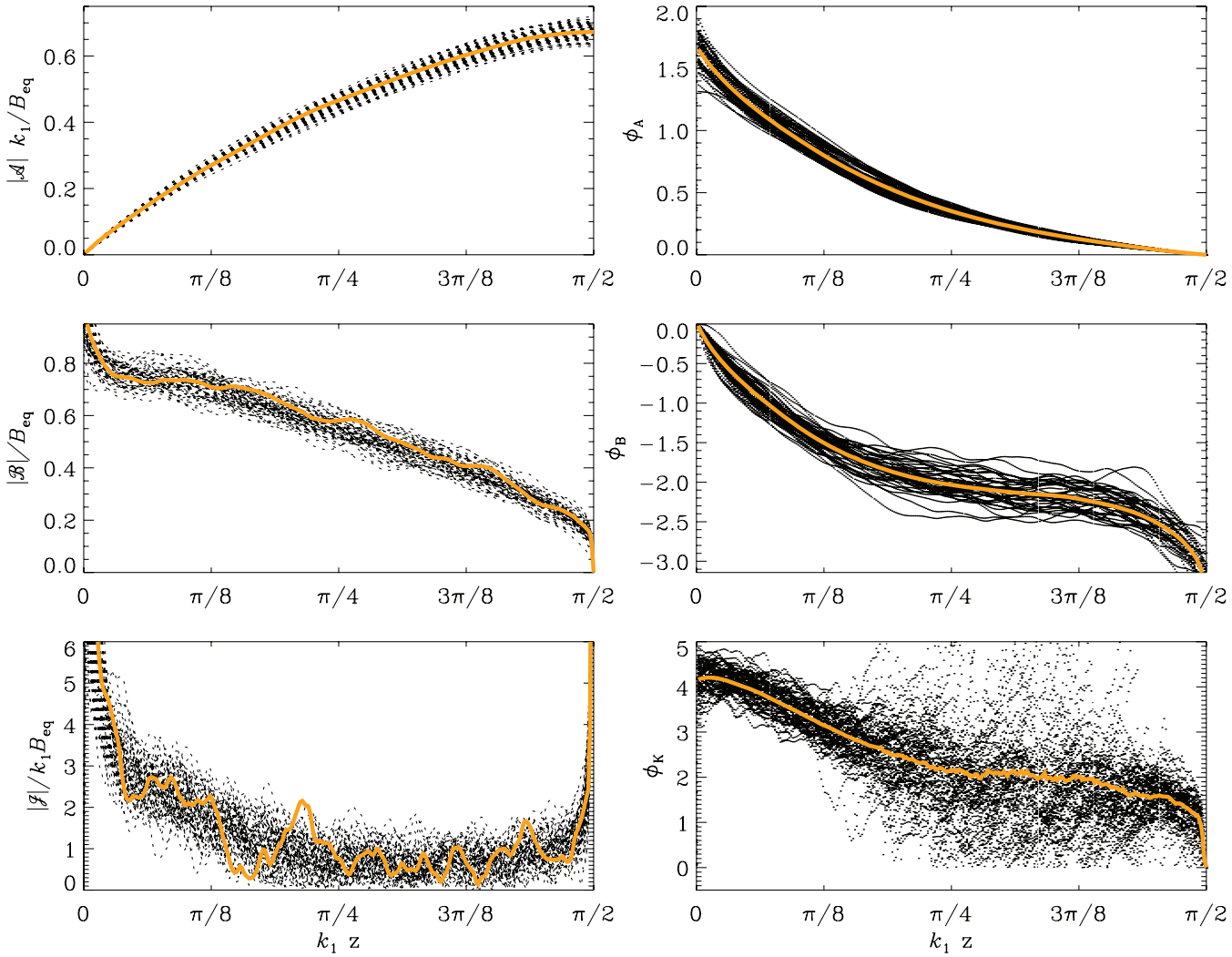

FIGURE 4 Moduli and phases of $\mathcal{A}$, $\mathcal{B}$, and $\mathcal{J}$ for Run A as a function of z. The fat orange lines denote the temporal averages

fields in complex notation as (Brandenburg 2017)

$$\mathcal{A} \equiv \overline{A}_x + i\overline{A}_y = r_A(z)e^{i\phi_A(z)-i\omega t}, \tag{5}$$

$$i\partial\mathcal{A} = \mathcal{B} \equiv \overline{B}_x + i\overline{B}_y = r_B(z)e^{i\phi_B(z)-i\omega t}, \tag{6}$$

$$i\partial\mathcal{B} = \mathcal{J} \equiv \overline{J}_x + i\overline{J}_y = r_J(z)e^{i\phi_J(z)-i\omega t}. \tag{7}$$

Thus, at each time, the complex quantities $\mathcal{A}$, $\mathcal{B}$, and $\mathcal{J}$ experience a certain phase shift. However, since we have a PC boundary condition with $\mathcal{A} = 0$ on $z=0$, we can subtract the phase at $z=0$ at each time and overplot the results in a single plot. Likewise for $\mathcal{B}$, which vanishes on the VF condition at $k_1 z = \pi/2$, we subtract here the phase at $k_1 z = \pi/2$ and overplot. For $\mathcal{J}$, no such condition exists, but we still get a reasonable result by subtracting the phase at $z=0$ at each time. For the moduli of $\mathcal{A}$, $\mathcal{B}$, and $\mathcal{J}$, no complications arise. The results for the nonlinearly saturated fields are plotted in Figure 4, normalized by $B_{\rm eq}/k_1$, $B_{\rm eq}$, and $B_{\rm eq}\ k_1$, respectively.

Again, the current density appears more noisy than the quantities in any of the other plots. Somewhat more surprising this time is the fact that $|\mathcal{J}|$ is mostly flat, except in the proximity of both boundaries. This could possibly hint at numerical artifacts related to the fact that we have the PC and VF boundary conditions as symmetry conditions, which also affect second and higher derivatives in unwanted ways. As shown in Brandenburg (2017), such an approach still gives correct solutions, but they converge more slowly.

3.3 | Comparison with the analytic α^2 dynamo

The solution of the α^2 dynamo with constant α and turbulent magnetic diffusivity $\eta_{\rm t}$, and with PC boundary conditions on $z=0$ and a VF condition on $z=\pi/2$ reads (Brandenburg 2017)

$$\mathcal{A}(z,t) = \mathcal{A}_0(e^{ik_+ z} - e^{ik_- z})e^{-i\omega t}, \tag{8}$$

where $\mathcal{A}_0$ is an amplitude factor, which is undefined in linear theory. Furthermore,

$$k_+/k_1 \approx 0.10161896 - 0.51915398i, \tag{9}$$

$$k_-/k_1 \approx -2.6522693 + 0.51915398i, \tag{10}$$

are complex wavenumbers, and

$$\omega/\eta_{\rm t}k_1^2 \approx -1.4296921 \tag{11}$$

is the frequency for the marginally excited dynamo with the critical value $\alpha \approx 2.5506504\eta_{\rm t}k_1$.

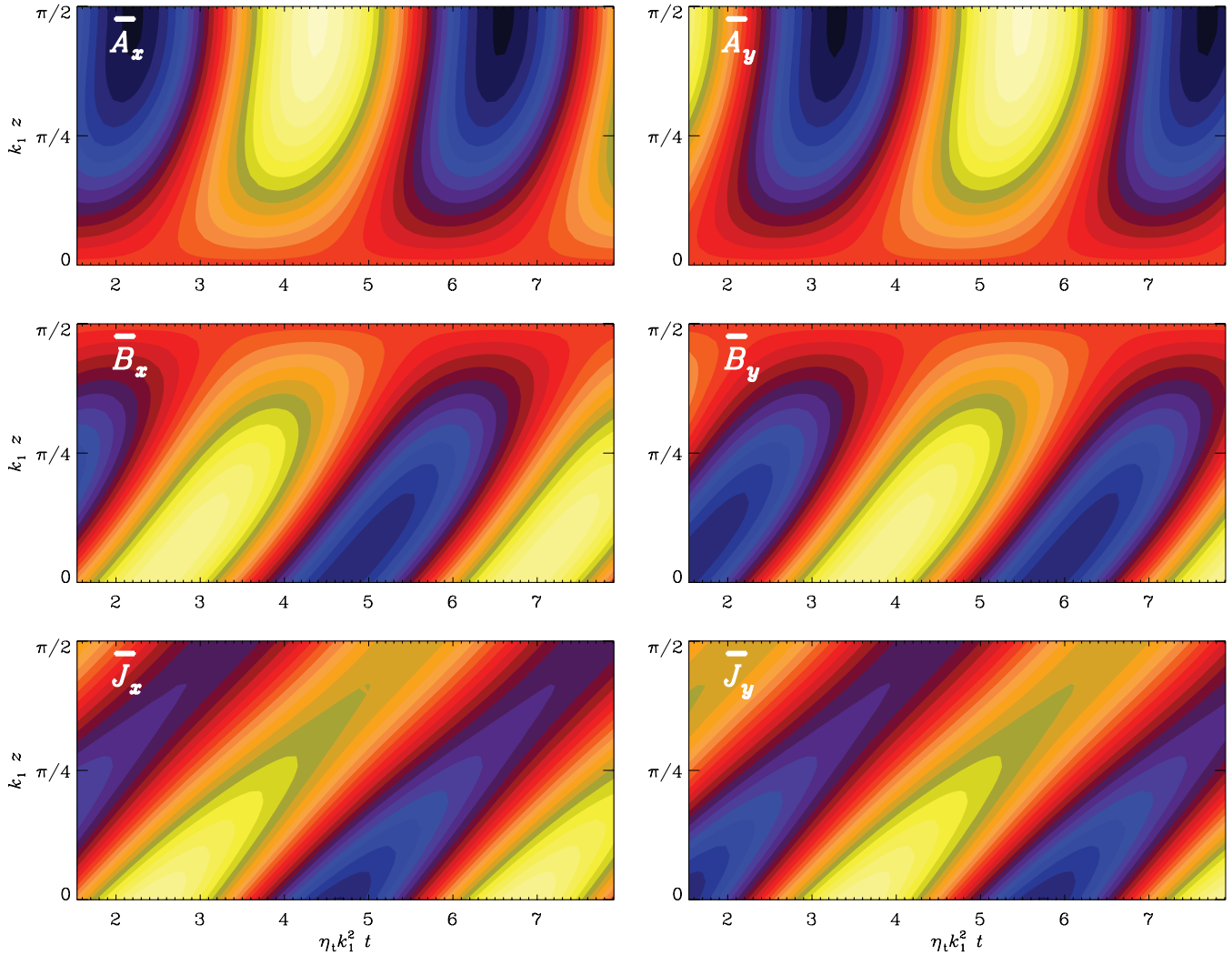

FIGURE 5 Butterfly diagrams of $\overline{A}_x$, $\overline{A}_y$, $\overline{B}_x$, $\overline{B}_y$, $\overline{J}_x$, and $\overline{J}_y$ for the α^2 mean-field dynamo. The color bars are similar to those in Figure 3, except that the amplitude is undetermined in linear theory

In Figure 5, we plot butterfly diagrams of the real and imaginary parts of $\mathcal{A}(z,t)$, $\mathcal{B}(z,t)$, and $\mathcal{J}(z,t)$ for this analytic solution. In comparison with Figure 3, the main difference is that in the simulation the pattern develops a large migration speed at large values of z, that is, the butterfly wings are nearly vertical. This is not seen in the analytic model. Apart from this, however, the cycle period is similar: $\omega = 1.16\eta_t k_1^2$ in the simulation compared with $1.43\eta_t k_1^2$ in the analytic model, which is about 23% larger.

In Figure 6 we show the absolute values and phases of $\mathcal{A}$, $\mathcal{B}$, and $\mathcal{J}$ for this α^2 dynamo as a function of z. All these dependencies are similar to those in the three-dimensional simulations; see Figure 4. However, there are also systematic differences, but it is unclear to what extent those are related to the fact that these simulations are nonlinear, and that the effective α and η_t acting in this three-dimensional simulations may not be constant in space. There may be many other such reasons for the disagreement.

To find out how supercritical the mean-field dynamo in the simulation is, we estimate the modulus of α as $\alpha_0 = u_{\rm rms}/3$ (Sur et al. 2008) and compute the dynamo number as $C_\alpha = \alpha_0/\eta_{t0}k_1 = k_f/k_1 = 4$. Thus, the dynamo is less than 1.6 times supercritical, which is not much. It would be interesting to compare with solutions that are either more supercritical or less supercritical, but this will not be carried out in the present work. Instead, in the rest of this work, we focus on magnetic helicity fluxes.

3.4 | Magnetic helicity balance

We now discuss the magnetic helicity equation, which is obtained by dotting Equation (1) with $\boldsymbol{B}$ and adding the curl of Equation (1) dotted with $\boldsymbol{A}$. The result is

$$\frac{\partial}{\partial t}\overline{\boldsymbol{A}\cdot\boldsymbol{B}} = -2\eta\overline{\boldsymbol{J}\cdot\boldsymbol{B}} - \frac{\partial}{\partial z}(\overline{\boldsymbol{E}\times\boldsymbol{A}} + \overline{\Phi\boldsymbol{B}}), \qquad (12)$$

where $\boldsymbol{E} = \eta\boldsymbol{J} - \boldsymbol{U}\times\boldsymbol{B}$ is the electric field and $\Phi = -\eta\boldsymbol{\nabla}\cdot\boldsymbol{A}$ is a scalar potential that results here from the facts that η is constant and the diffusion term on the right-hand side in Equation (1) can be written as $\nabla^2\boldsymbol{A} = -\boldsymbol{J} + \boldsymbol{\nabla}\boldsymbol{\nabla}\cdot\boldsymbol{A}$. Next, we consider the evolution of the magnetic helicity of the mean field, $\overline{\boldsymbol{A}}\cdot\overline{\boldsymbol{B}}$, and subtract it from Equation (12) to obtain the evolution equation of the magnetic helicity of the fluctuating

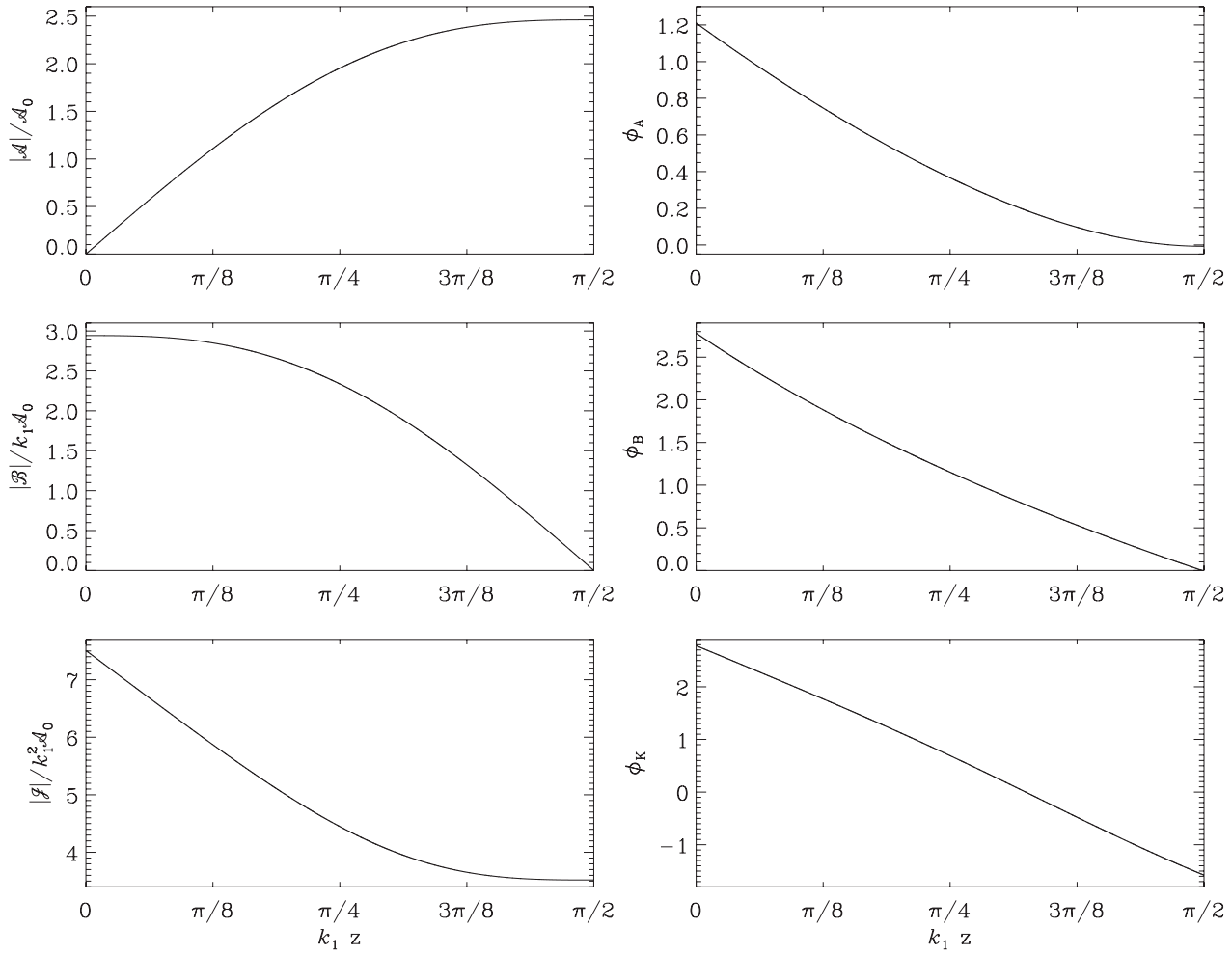

FIGURE 6 Moduli and phases of $\mathcal{A}$, $\mathcal{B}$, and $\mathcal{J}$ for the α^2 of Brandenburg (2017) as a function of z

fields, $\boldsymbol{a} = \boldsymbol{A} - \overline{\boldsymbol{A}}$ and $\boldsymbol{b} = \boldsymbol{B} - \overline{\boldsymbol{B}}$, using

$$\overline{\boldsymbol{a} \cdot \boldsymbol{b}} = \overline{\boldsymbol{A} \cdot \boldsymbol{B}} - \overline{\boldsymbol{A}} \cdot \overline{\boldsymbol{B}}, \tag{13}$$

where we have made use of the Reynolds rules for horizontal averages. The evolution equation for $\overline{\boldsymbol{A}}$ can be written in the form

$$\frac{\partial \overline{\boldsymbol{A}}}{\partial t} = \overline{\boldsymbol{U}} \times \overline{\boldsymbol{B}} + \overline{\boldsymbol{\mathcal{E}}} - \eta \overline{\boldsymbol{J}} - \nabla \overline{\Phi}, \tag{14}$$

where $\overline{\Phi} = -\eta \nabla \cdot \overline{\boldsymbol{A}} = -\eta \partial \overline{A}_z / \partial z$, and the $\eta \overline{\boldsymbol{J}}$ term describes the microphysical diffusion of the mean field, which is usually small in comparison with turbulent magnetic diffusion. The traditional α effect and turbulent diffusion are all modeled through the $\overline{\boldsymbol{\mathcal{E}}}$ term as $\overline{\boldsymbol{\mathcal{E}}} = \alpha \overline{\boldsymbol{B}} - \eta_t \overline{\boldsymbol{J}}$, but no such specification needs to be made at this point. Thus, we have

$$\frac{\partial}{\partial t}(\overline{\boldsymbol{A}} \cdot \overline{\boldsymbol{B}}) = 2\overline{\boldsymbol{\mathcal{E}}} \cdot \overline{\boldsymbol{B}} - 2\eta \overline{\boldsymbol{J}} \cdot \overline{\boldsymbol{B}} - \frac{\partial}{\partial z}(\overline{\boldsymbol{E}} \times \overline{\boldsymbol{A}} + \overline{\Phi}\, \overline{\boldsymbol{B}} - \overline{\boldsymbol{\mathcal{E}}} \times \overline{\boldsymbol{A}}), \tag{15}$$

where $\overline{\boldsymbol{E}} = \eta \overline{\boldsymbol{J}} - \overline{\boldsymbol{U}} \times \overline{\boldsymbol{B}}$ is the electric field resulting from the mean fields, but without the contribution from the fluctuations that are already included in the $\overline{\boldsymbol{\mathcal{E}}}$ term. By subtracting Equation (15) from Equation (12), we obtain

$$\frac{\partial}{\partial t}\overline{\boldsymbol{a} \cdot \boldsymbol{b}} = -2\overline{\boldsymbol{\mathcal{E}}} \cdot \overline{\boldsymbol{B}} - 2\eta \overline{\boldsymbol{j} \cdot \boldsymbol{b}} - \frac{\partial}{\partial z}(\overline{\boldsymbol{e} \times \boldsymbol{a}} + \overline{\phi \boldsymbol{b}} + \overline{\boldsymbol{\mathcal{E}}} \times \overline{\boldsymbol{A}}), \tag{16}$$

where

$$\overline{\boldsymbol{j} \cdot \boldsymbol{b}} = \overline{\boldsymbol{J} \cdot \boldsymbol{B}} - \overline{\boldsymbol{J}} \cdot \overline{\boldsymbol{B}} \tag{17}$$

is the current helicity of the small-scale field,

$$\overline{\boldsymbol{e} \times \boldsymbol{a}} = \overline{\boldsymbol{E} \times \boldsymbol{A}} - \overline{\boldsymbol{E}} \times \overline{\boldsymbol{A}} \tag{18}$$

is the magnetic helicity flux of the small-scale field, and

$$\overline{\phi \boldsymbol{b}} = \overline{\Phi \boldsymbol{B}} - \overline{\Phi}\, \overline{\boldsymbol{B}} \tag{19}$$

is a contribution to the magnetic helicity flux that results from the particular gauge of the small-scale field.

In Figures 7 and 8, we compare the profiles of magnetic helicity, current helicity, and the magnetic helicity fluxes for Runs A and B with $\mathrm{Re_M} = 180$ and 370, respectively. For normalization purposes, we have defined

$$H_{\mathrm{m0}} = \int_0^{\pi/2} \overline{\boldsymbol{B}}^2 \mathrm{d}z, \tag{20}$$

$$C_{\mathrm{f0}} = k_{\mathrm{f}} B_{\mathrm{eq}}^2, \tag{21}$$

$$F_{\mathrm{m0}} = \eta_{\mathrm{t0}} k_1^2 \int_0^{\pi/2} \overline{\boldsymbol{B}}^2 \mathrm{d}z. \tag{22}$$

Not surprisingly, the largest contribution to the magnetic helicity density comes from the large-scale field. This is also reasonably well reproduced by the mean-field model; see Figure 9.

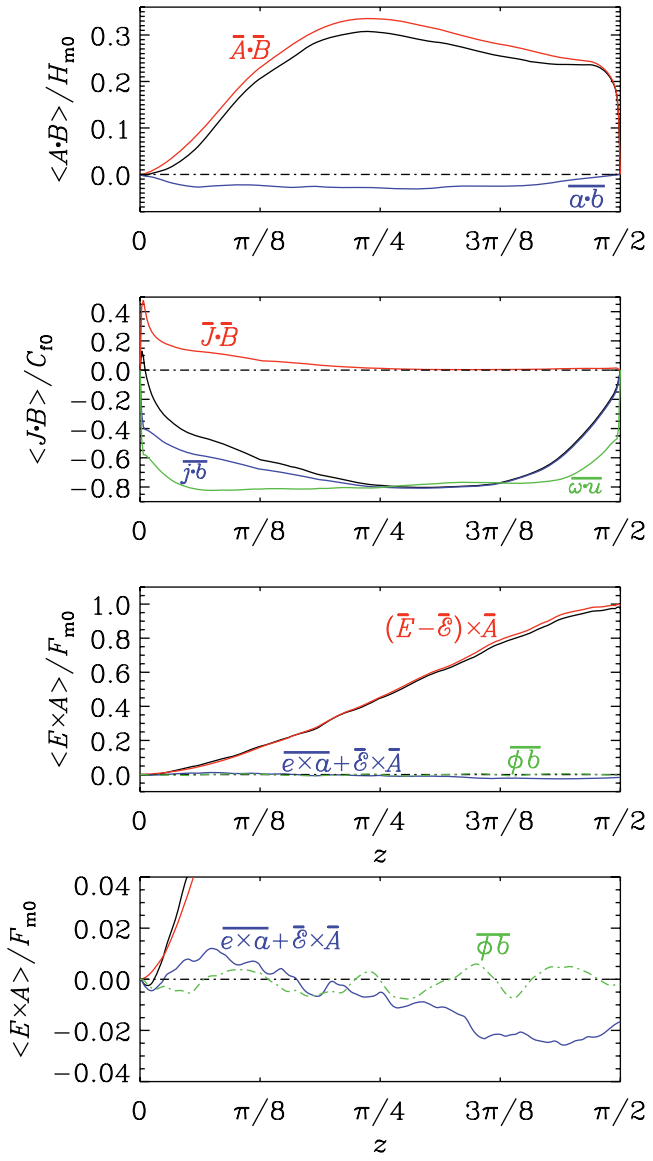

FIGURE 7 Magnetic helicity, current helicity, and magnetic helicity fluxes for Run A with $\mathrm{Re_M} = 180$. In the second panel, the kinetic helicity is shown in green and is found to be of similar magnitude to the current helicity of the small-scale field. The last two panels are similar except that a smaller range near zero is shown. Here, the green line denotes $\overline{\phi b}_z$, which is seen to fluctuate around zero

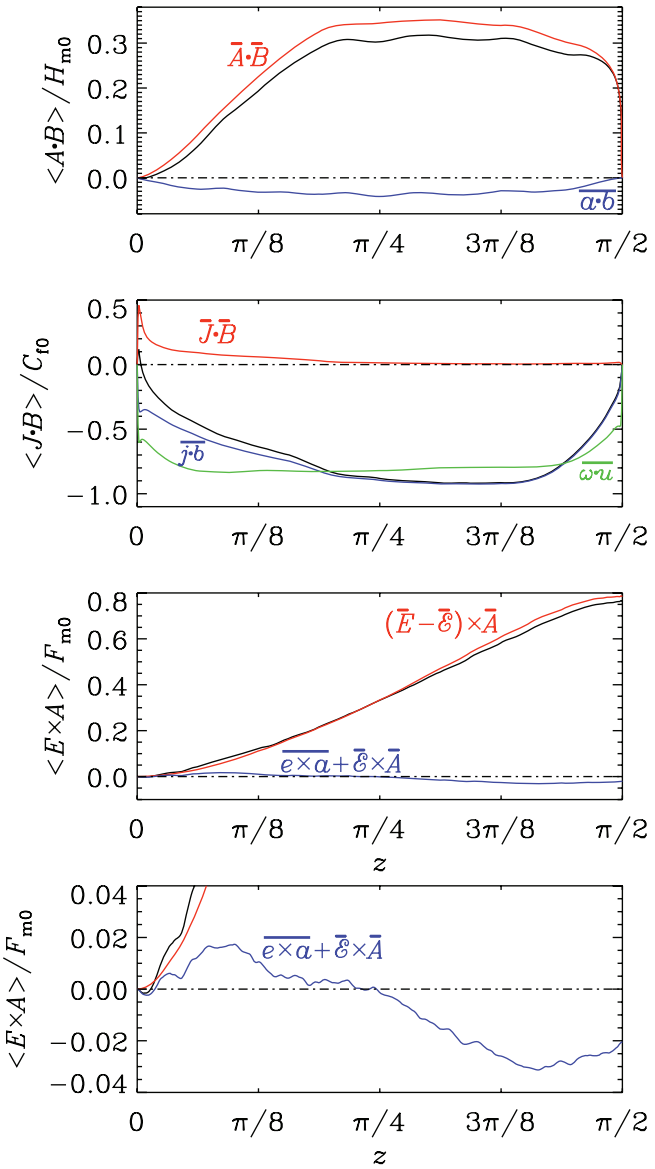

FIGURE 8 Similar to Figure 7, but for Run B with $\mathrm{Re_M} = 370$

Again, not surprisingly, the current helicity is dominated by the small-scale parts with $\overline{\boldsymbol{j}\cdot\boldsymbol{b}}/k_{\rm f}B_{\rm eq}^2$ being reasonably close to -1. The current helicity of the small-scale field is also close to the kinetic helicity density, similar to what was found for perfectly homogeneous dynamos in periodic domains (Brandenburg 2001). More surprising is the fact that most of the magnetic helicity flux comes from the large-scale magnetic field, and very little from the small-scale field. However, it may be interesting that the contribution from the small-scale field is similar for Runs A and B, that is, $\overline{\boldsymbol{E}\times\boldsymbol{A}}/F_{\rm m0} \approx -0.03$ in both cases, and perhaps even slightly larger for Run B. It will be interesting to evaluate these terms at even higher resolution and for higher magnetic Reynolds numbers. It is conceivable that the fluxes from the large-scale field continue to decline, but that those of the small-scale field remain constant or increase and might eventually be equal to the contributions from the small-scale fields.

3.5 | Dependence on $\mathrm{Re_M}$

To study the dependence of the solutions on $\mathrm{Re_M}$, it is useful to compute the energy contained in the mean field, which is essentially the same as our normalization constant $H_{\rm m0}$. In Table 2, we list those values for all four runs and normalize by ${B_{\rm eq}}^2/k_1$, which itself is almost the same in all four cases.

We see that there is a systematic decline in $H_{\rm m0}\,k_1/{B_{\rm eq}}^2$ as $\mathrm{Re_M}$ increases. Thus, these models do not yet appear to be in the asymptotic regime. Investigating these values for longer simulations and at larger values of $\mathrm{Re_M}$ will be important and is also needed for calculating reliable error bars.

3.6 | Comparison with Run G

Run G had a vertical gradient in the helicity density, while the turbulent intensity was approximately independent of z. It

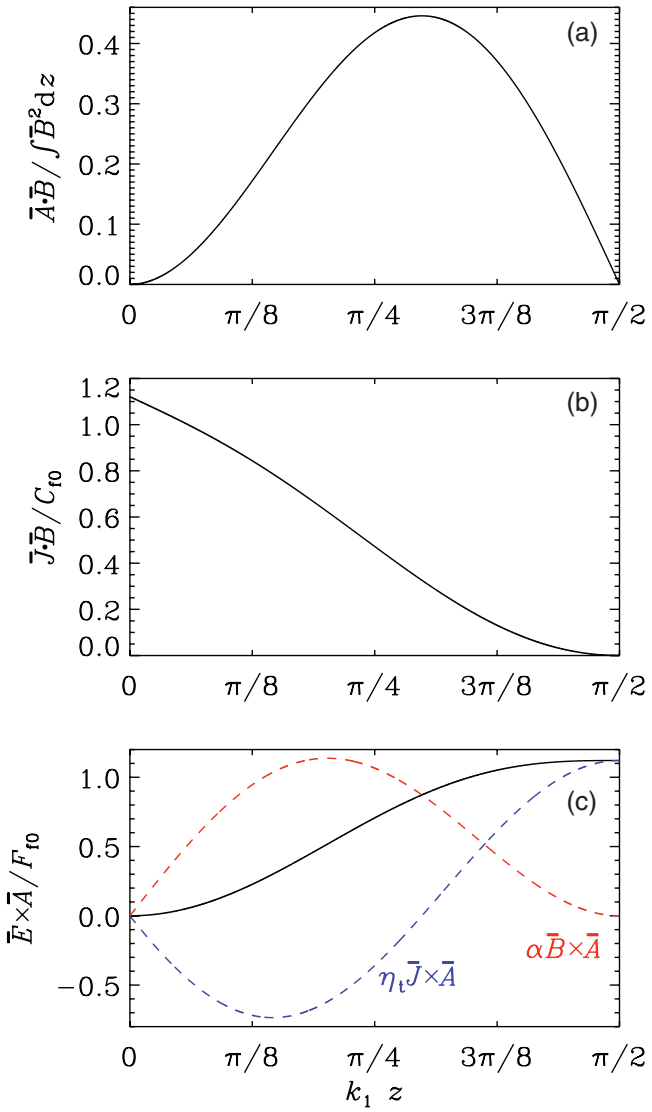

FIGURE 9 Magnetic and current helicity profiles as well as magnetic helicity fluxes in the mean-field α^2 dynamo

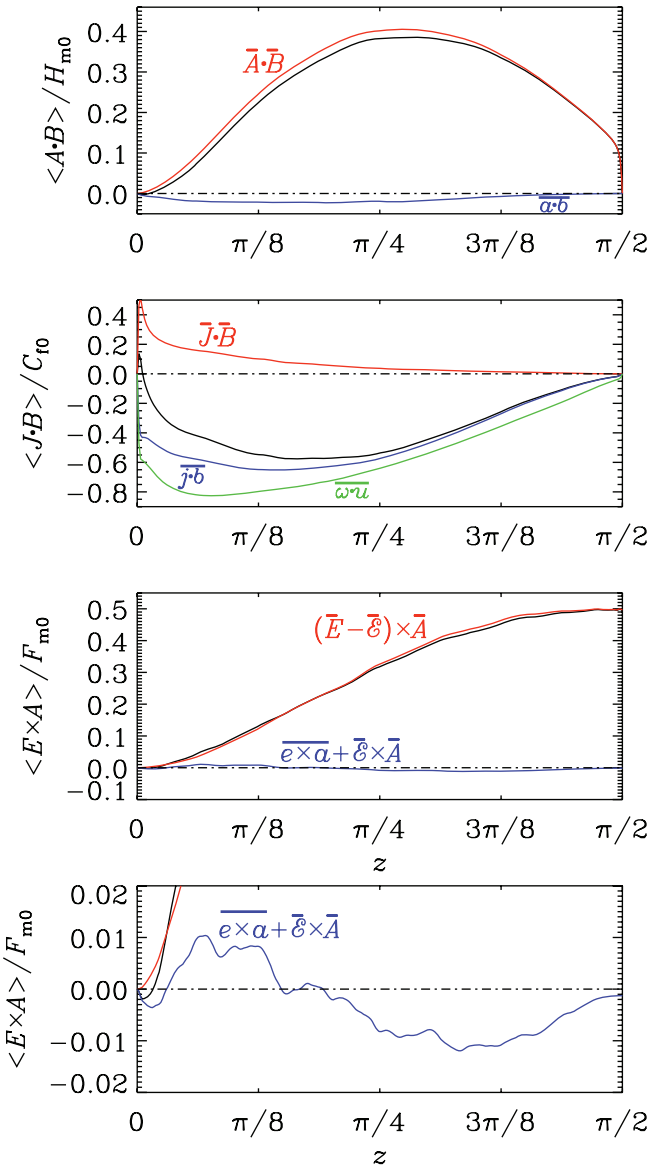

FIGURE 10 Similar to Figure 7, but for Run G with $\mathrm{Re_M}=170$

TABLE 2 Comparison of $H_{\rm m0}$, normalized by $B_{\rm eq}{}^2/k_1$, for all of our runs. For Run C, only a lower limit is given, because it is still too short

Run	$\mathrm{Re_M}$	Mesh	$H_{\rm m0}\,k_1/B_{\rm eq}{}^2$
G	170	288^3	0.60
A	180	288^3	0.51
B	370	576^3	0.36
C	750	1152^3	>0.02

is possible that such a gradient in the kinetic helicity, $\overline{\boldsymbol{\omega}\cdot\boldsymbol{u}}$, where $\boldsymbol{\omega}=\boldsymbol{\nabla}\times\boldsymbol{u}$ is the vorticity, would produce a similar gradient both in $\overline{\boldsymbol{j}\cdot\boldsymbol{b}}$ and in $\overline{\boldsymbol{a}\cdot\boldsymbol{b}}$, and thereby a magnetic helicity flux proportional to $-\nabla\overline{\boldsymbol{a}\cdot\boldsymbol{b}}$, as proposed by Hubbard & Brandenburg (2011). This does not seem to be the case and the magnetic helicity flux for the small-scale field does even go to zero near the upper boundary; see the last panel of Figure 10. Some other features in the nature of the small-scale turbulence may be needed that have not yet been identified.

4 | CONCLUSIONS

The present work has shown that turbulent dynamos with homogeneous helical forcing, but different boundary conditions on the lower and upper boundaries, lead to dynamo waves and magnetic helicity fluxes—similar to what is expected based on a mean-field model. Both mean-field models and simulations are similar in many respects and agree qualitatively within 23% in terms of the cycle period, but there are differences in the shape of the magnetic field and current density profiles.

The magnetic helicity profiles are strongly dominated by the large-scale magnetic field. This is somewhat disappointing in the sense that, to alleviate the catastrophic quenching problem discussed in the introduction, we expect the magnetic helicity fluxes to be dominated by small-scale contributions. On the other hand, it may be this magnetic helicity of the large-scale field that contributes to the mysterious sign

reversal found originally in the solar wind (Brandenburg et al. 2011). If this is correct, it may indicate that even in the Sun, the catastrophic quenching problem has not quite gone away yet.

Compared with Run G, which has a gradient in the kinetic helicity profile, we saw that it does not lead to major differences, suggesting that small-scale magnetic helicity transport from a downward gradient of magnetic helicity density is not very efficient in this model. It may therefore be useful to reconsider some of the earlier setups that have been studied to measure magnetic helicity fluxes in dynamo simulations. Mitra et al. (2010) considered a model between perfectly conducting boundaries, while Hubbard & Brandenburg (2010) considered a model with a poorly conducting halo. Finally, Del Sordo et al. (2013) studied a model where both advection from a wind and a downward gradient of magnetic helicity contributed to the flux of magnetic helicity. Comparative studies of the magnetic helicity fluxes from the small-scale magnetic field will be the subject of a separate publication.

ACKNOWLEDGMENTS

This research was supported in part by the Astronomy and Astrophysics Grants Program of the National Science Foundation (grant 1615100), and the University of Colorado through its support of the George Ellery Hale visiting faculty appointment. I acknowledge the allocation of computing resources provided by the Swedish National Allocations Committee at the Center for Parallel Computers at the Royal Institute of Technology in Stockholm.

REFERENCES

Bhat, P., Subramanian, K., & Brandenburg, A. 2016, *MNRAS*, *461*, 240.
Blackman, E. G., & Brandenburg, A. 2002, *ApJ*, *579*, 359.
Brandenburg, A. 2001, *ApJ*, *550*, 824.
Brandenburg, A. 2017, *A&A*, *598*, A117.
Brandenburg, A., & Dobler, W. 2001, *A&A*, *369*, 329.
Brandenburg, A., Dobler, W., & Subramanian, K. 2002, *Astron. Nachr.*, *323*, 99.
Brandenburg, A., Candelaresi, S., & Chatterjee, P. 2009, *MNRAS*, *398*, 1414 (BCC).
Brandenburg, A., Subramanian, K., Balogh, A., & Goldstein, M. L. 2011, *ApJ*, *734*, 9.
Candelaresi, S., & Brandenburg, A. 2013, *Phys. Rev. E*, *87*, 043104.
Candelaresi, S., Hubbard, A., Brandenburg, A., & Mitra, D. 2011, *Phys. Plasmas*, *18*, 012903.
Cattaneo, F., & Hughes, D. W. 1996, *Phys. Rev. E*, *54*, R4532.
Cattaneo, F., & Vainshtein, S. I. 1991, *ApJ*, *376*, L21.
Del Sordo, F., Guerrero, G., & Brandenburg, A. 2013, *MNRAS*, *429*, 1686.
Field, G. B., & Blackman, E. G. 2002, *ApJ*, *572*, 685.
Gruzinov, A. V., & Diamond, P. H. 1994, *Phys. Rev. Lett.*, *72*, 1651.
Gruzinov, A. V., & Diamond, P. H. 1995, *Phys. Plasmas*, *2*, 1941.
Gruzinov, A. V., & Diamond, P. H. 1996, *Phys. Plasmas*, *3*, 1853.
Hubbard, A., & Brandenburg, A. 2010, *Geophys. Astrophys. Fluid Dyn.*, *104*, 577.
Hubbard, A., & Brandenburg, A. 2011, *ApJ*, *727*, 11.
Ji, H. 1999, *Phys. Rev. Lett.*, *83*, 3198.
Kleeorin, N. I., & Ruzmaikin, A. A. 1982, *Magnetohydrodynamics*, *18*, 116.
Mitra, D., Candelaresi, S., Chatterjee, P., Tavakol, R., & Brandenburg, A. 2010, *Astron. Nachr.*, *331*, 130.
Parker, E. N. 1955, *ApJ*, *122*, 293.
Pouquet, A., Frisch, U., & Léorat, J. 1976, *J. Fluid Mech.*, *77*, 321.
Rüdiger, G., & Hollerbach, R. 2004, *The Magnetic Universe*, Wiley-VCH, Weinheim (New York).
Ruzmaikin, A. A. 1981, *Comments Astrophys.*, *9*, 85.
Seehafer, N. 1996, *Phys. Rev. E*, *53*, 1283.
Steenbeck, M., & Krause, F. 1969, *Astron. Nachr.*, *291*, 49.
Steenbeck, M., Krause, F., & Rädler, K.-H. 1966, *Z. Naturforsch.*, *21a*, 369 See also the translation in Roberts & Stix, The turbulent dynamo, Tech. Note 60, NCAR, Boulder, Colorado (1971).
Subramanian, K. 2002, *Bull. Astron. Soc. India*, *30*, 715.
Subramanian, K., & Brandenburg, A. 2014, *MNRAS*, *445*, 2930.
Sur, S., Brandenburg, A., & Subramanian, K. 2008, *MNRAS*, *385*, L15.
Tavakol, R. K. 1978, *Nature*, *276*, 802.
Vainshtein, S. I., & Cattaneo, F. 1992, *ApJ*, *393*, 165.

How to cite this article: Brandenburg A. Magnetic helicity and fluxes in an inhomogeneous α^2 dynamo. *Astron. Nachr.* 2018;339:631–640. https://doi.org/10.1002/asna.201913604